Digest Journal of Nanomaterials and Biostructures Vol. 20, No. 4, October-December 2025, p. 1507-1517

Improvement of anti-corrosion behavior of micro-arc oxidation layers with natural zeolite particles addition into electrolytes

Y. Zhang, S. Sun, E. Xue, J. Shang *
School of Materials Science and Engineering, Liaoning University of Technology, Jinzhou 121001, China

This study explores the improvement of corrosion resistance in micro-arc oxidation (MAO) layers through the incorporation of natural zeolite particles (NZP). The findings indicate that the addition of 20 g/L NZP effectively reduced the surface porosity from 15.78% to 7.38%. Furthermore, the impedance modulus (|Z|) of the prepared layers increased by three orders of magnitude, reaching 3.72×10^3 Ω·cm^2, while the self-corrosion current density decreased six orders of magnitude, to 1.22×10^{-6} A/cm^2. After immersion in a 3.5wt.% NaCl solution for 168 hours, the NZP-containing layers exhibited a notable reduction in $Mg(OH)_2$ content.

(Received September 3, 2025; Accepted December 12, 2025)

Keywords: Mg alloys, Particles, Surfaces, Corrosion

1. Introduction

Magnesium (Mg) can be used in automotive, aerospace, communications, and healthcare field due to its low density, and high strength, biocompatibility, and recyclability[1-2]. However, the high reactivity limits the broader application of Mg alloys[3]. Micro-arc oxidation (MAO) is considered as a promising method because of their high hardness and strong adhesion with matrix are commonly applied to non-ferrous metals like Al, Mg, Ti, and Nb[4]. Despite these advantages, the porous nature of MAO layers allows corrosive media to penetrate, leading to substrate degradation and limiting their effectiveness[5].

Recent attention has focused on metal-organic frameworks (MOFs) for their cage-like structures, which enhance corrosion resistance. Jiang et al.[6] improved Mg alloy corrosion resistance by growing a ZIF-8 coating on MAO-treated AZ91, reducing the self-corrosion current density from 10^{-5} A/cm^2 to 10^{-9} A/cm^2. Chen et al.[7] used an in-situ method to prepare Mg-Al-Zn layered double hydroxide (LDH) on a MAO/ZIF-8 composite, reducing the current density to 1.48×10^{-8} A/cm^2. Chen et al.[8] also incorporated cerium-containing zeolites into the MAO process, forming a self-healing layer that raised impedance from 2.08×10^5 to 7.48×10^7 Ω·cm^2 after 96 hours in NaCl solution. Although synthetic zeolites show strong performance, their large-scale use is limited by high costs, environmental concerns, and resource scarcity. This study aims to enhance MAO coating corrosion resistance by incorporating natural zeolite particles (NZP) directly into the

* Corresponding author: shangjian@lnut.edu.cn
https://doi.org/10.15251/DJNB.2025.204.1507

process. Surface morphology, porosity, and electrochemical evaluations demonstrate that NZP significantly improves the corrosion protection of MAO layers, offering a sustainable solution for enhanced durability.

2. Experimental methods and characterization

The AZ31 magnesium alloy was cut into 20×20×4 mm specimens and then polished using SiC paper from 320 # to 1500 #. The samples were then ultrasonically cleaned in anhydrous ethanol to remove grease and dried by hot air. The micro-arc oxidation (MAO) was carried out by a pulse power supply (WHD-30, China) under constant current mode (0.8 A current, 500 Hz frequency, 20% duty cycle, and 10 min) . The electrolyte solution are 10 g/L $Na_2SiO_3 \cdot 9H_2O$, 6 g/L $(NaPO_3)_6$, 4 g/L NaOH, 3 g/L EDTA-2Na, and varying concentrations (0 to 20 g/L) of natural zeolite powder (NZP, average particle size: 7.62 μm) . The samples were labeled as NZP-0g, NZP-10g, NZP-15g, and NZP-20g.

The phase composition of prepared layer was tested by X-ray diffraction (XRD, D/max-2500/PC, Japan). The surface morphology and elemental composition were characterized by scanning electron microscopy (FE-SEM, Sigma 500, Germany) equipped with energy dispersive X-ray spectroscopy (EDS, AZtec X-Max 50, UK). The elemental composition of prepared layer was studied by X-ray photoelectron spectroscopy (ESCALAB 250Xi) at 400 W and 14 kV. Porosity was measured using Image-J software. The polarization curve and electrochemical impedance spectroscopy (EIS), were tested by IVIUM electrochemical workstation (Xri, Netherlands) with three-eletrode system with 1 cm^2 exposed area. The saturated calomel reference electrode, a platinum foil counter electrode, and the NZP-coated sample as the working electrode. The natural immersion tests was conducted in a NaCl solution for 168 hours, and the corroded samples were characteized by XRD, SEM, and EDS analyses.

3. Results and discussion

Fig.1 are the morphology and pore distribution of different samples at 200× magnification. As shown in Fig.1a, when no natural zeolite particles (NZP) are added, the NZP-0g layer exhibits a large number of crater-like pores resembling "volcanic craters," with relatively high pore density and larger pore sizes. This characteristic porous structure results from the significant gas and plasma release during the MAO process. Such defects allow corrosive media to penetrate the layer, thereby reducing its corrosion resistance[9]. As depicted in Fig.1b, the NZP-10g layer exhibits a few bright white spots on the surface, and some smaller pores appear to be sealed. With increasing NZP content, the number of bright white spots further increases in Fig.1c-d for the NZP-15g and NZP-20g layers. In addition to NZP particles being incorporated into the MAO layer and sealing the micropores, some larger pores (4–6 μm) are also effectively closed. The pore distribution analysis in Fig.1 indicates that as the NZP content increases, not only does the number and size of surface pores in the MAO layer decrease, but the number and size of cracks also significantly reduce. Surface cracks in the MAO layer are attributed to the excess stress generated during the thermodynamic instability of the molten-to-solid transition. The addition of NZP particles into the prepared layer helps alleviate part of this stress, thereby reducing the number and size of cracks. ImageJ software analysis at a

threshold of 0–50 reveals that the porosity of NZP-0g, NZP-10g, NZP-15g, and NZP-20g coatings is 15.78%, 8.72%, 8.12%, and 7.40%, respectively. These results indicate that the MAO formation process can adsorb large particle size NZP and close its surface pores.The increase of NZP content can further reduce pores and cracks in MAO layer, and it is contributed to improvement of the corrosion resistance of oxide layer.

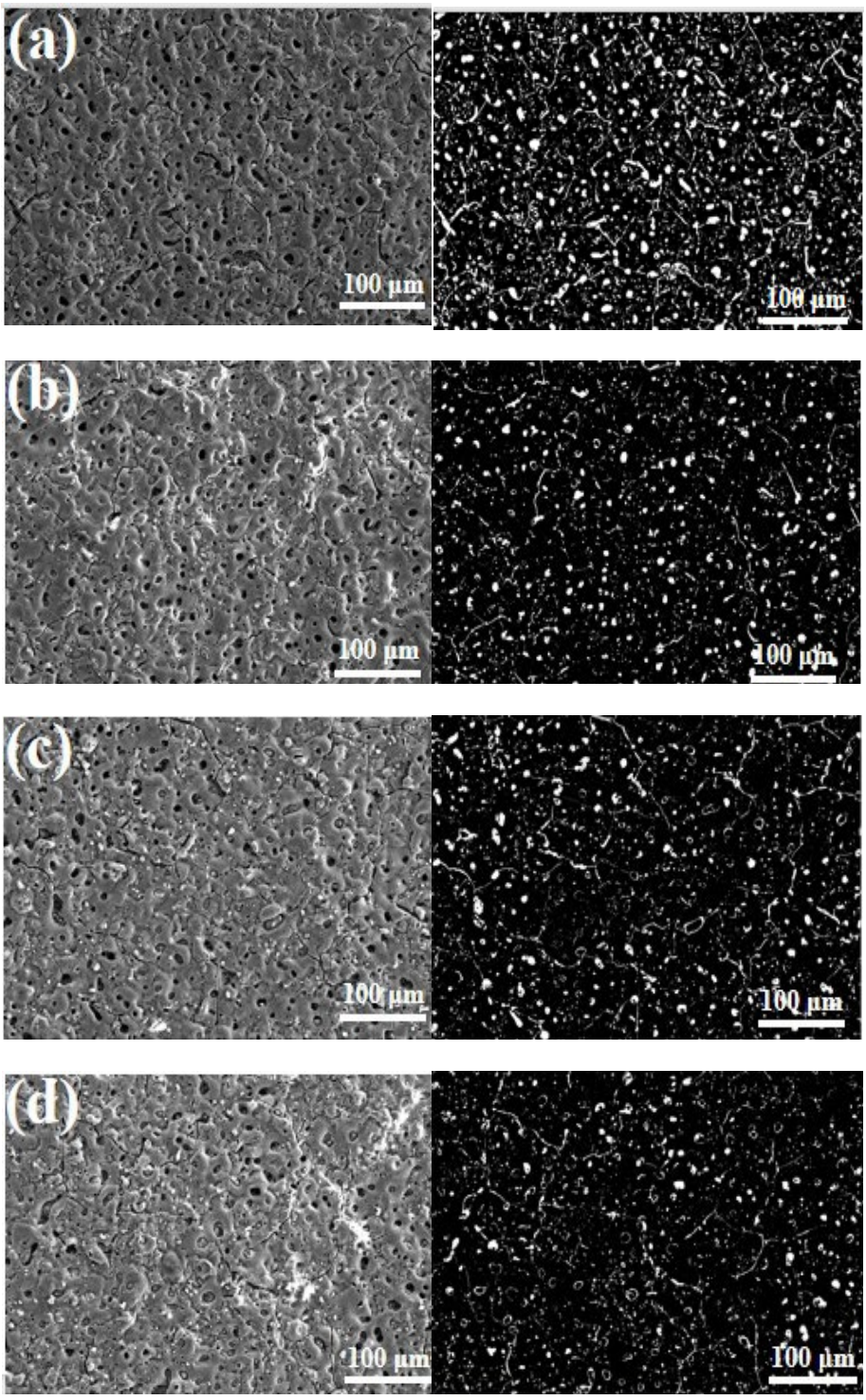

Fig. 1. SEM surface morphology and pore distribution of different MAO samples: (a) NZP-0, (b) NZP-10, (c) NZP-15, and (d) NZP-20.

Fig. 2 presents the SEM and XRD pattern of NZP. Fig.2a shows the SEM image of natural zeolite powder, revealing that the crushed and sieved zeolite particles exhibit an irregular block-like polyhedral morphology. The particle sizes generally range from 1 to 6 μm, with a few particles reaching 8–10 μm. Fig.2b displays the XRD pattern of the natural zeolite powder, indicating that it primarily consists of calcium aluminosilicate compounds, including $Al_{0.5}Si_{0.75}O_{2.25}\cdot xH_2O$, $CaSi_2O_4$, $CaAl_2O_4$, $CaCO_3$, and SiO_2.

Fig. 3 presents XRD patterns of different coatings and the XPS spectra of the NZP-15g sample. As shown in Fig.3a, the MAO coating primarily consists of α-Mg, MgO, Mg_2SiO_4, and $Ca_3Al_2Si_3O_{12}$. With increasing NZP content, the Mg substrate peaks at 36° and 62° gradually decreases, indicating enhanced coverage of the substrate by the MAO layer. Combined with the findings from Fig.1, this suggests that the coating pores are effectively filled with NZP, leading to increased coating density. Since the XRD results in Fig.3a do not show a distinct NZP phase compared to the NZP-0g coating, XPS analysis was conducted on the NZP-15g coating, which contains a moderate amount of NZP (Fig.3b–d). The full XPS spectrum (Fig.3b) confirms the apperance of Mg, Al, O, Ca, Si, and C element. The binding energies were determined using the NIST X-ray Photoelectron Spectroscopy Database. To further distinguish NZP, high-resolution spectral analysis was performed for the characteristic elements Ca and Si. The high-resolution Ca 2p spectrum (Fig.3c) exhibits peaks at 351.8 eV and 347.9 eV, and it is corresponded to Ca–O bonds and calcium aluminum silicate oxide (CASO). The Si 2p spectrum (Fig.3d) shows peaks at 101.8 eV and 99.1 eV. These results confirm the of NZP is in the MAO layer.

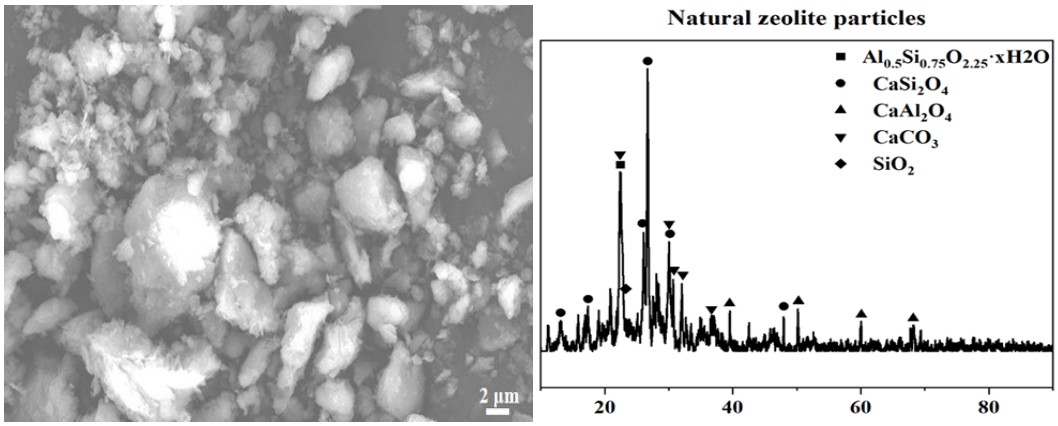

(a) *(b)*

Fig. 2. SEM and XRD pattern of natural zeolite powder particles.

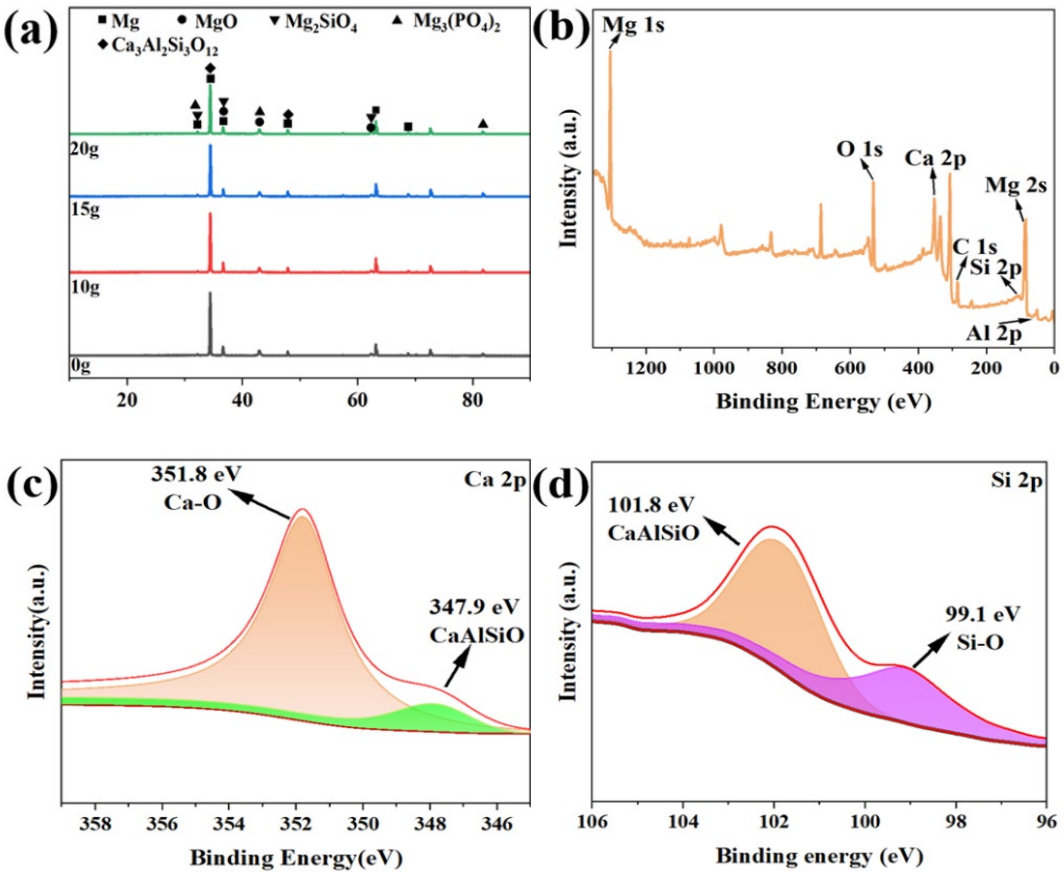

Fig. 3. XRD patterns of different MAO samples and XPS spectra of the NZP-15g sample.

Fig. 4 presents SEM and EDS analysis of different layer at 500× magnification. The SEM image of the NZP-0g coating (Fig.4a) reveals a surface characterized by numerous pores and cracks. These cracks are not only abundant and large in size but also show a tendency to interconnect. The EDS analysis of the NZP-0g coating indicates that its surface contains Mg, O, P, and Si. The surface morphology of the NZP-10g, NZP-15g, and NZP-20g coatings (Fig.4b-d) aligns with the observations in Fig.1. As the NZP content increases, pores of varying sizes in the MAO layer gradually become filled with NZP particles, with the number of sealed pores increasing accordingly. From EDS results for the NZP-10g, NZP-15g, and NZP-20g coatings, it can be seen that the surface presents Mg, O, P, Si, and Al. With increasing NZP content, enriched regions of Al and Si appear on the coating surface, and their locations correspond closely to the areas where NZP has sealed the pores, confirming the incorporation of NZP into prepared layer. For the NZP-15g coating, most pores are sealed except for a few larger ones. In the NZP-20g coating, all small pores are completely sealed, and some larger pores exceeding 10 μm in size are also filled. However, as shown in Fig.4d, the large pores sealed by NZP still exhibit slight gaps at the interface with the MAO surface. This encapsulation mechanism suggests that NZP is captured during the MAO layer formation, where molten material simultaneously adsorbs NZP into the coating and encapsulates it as the layer grows outward, ultimately leading to the closure of large pores.

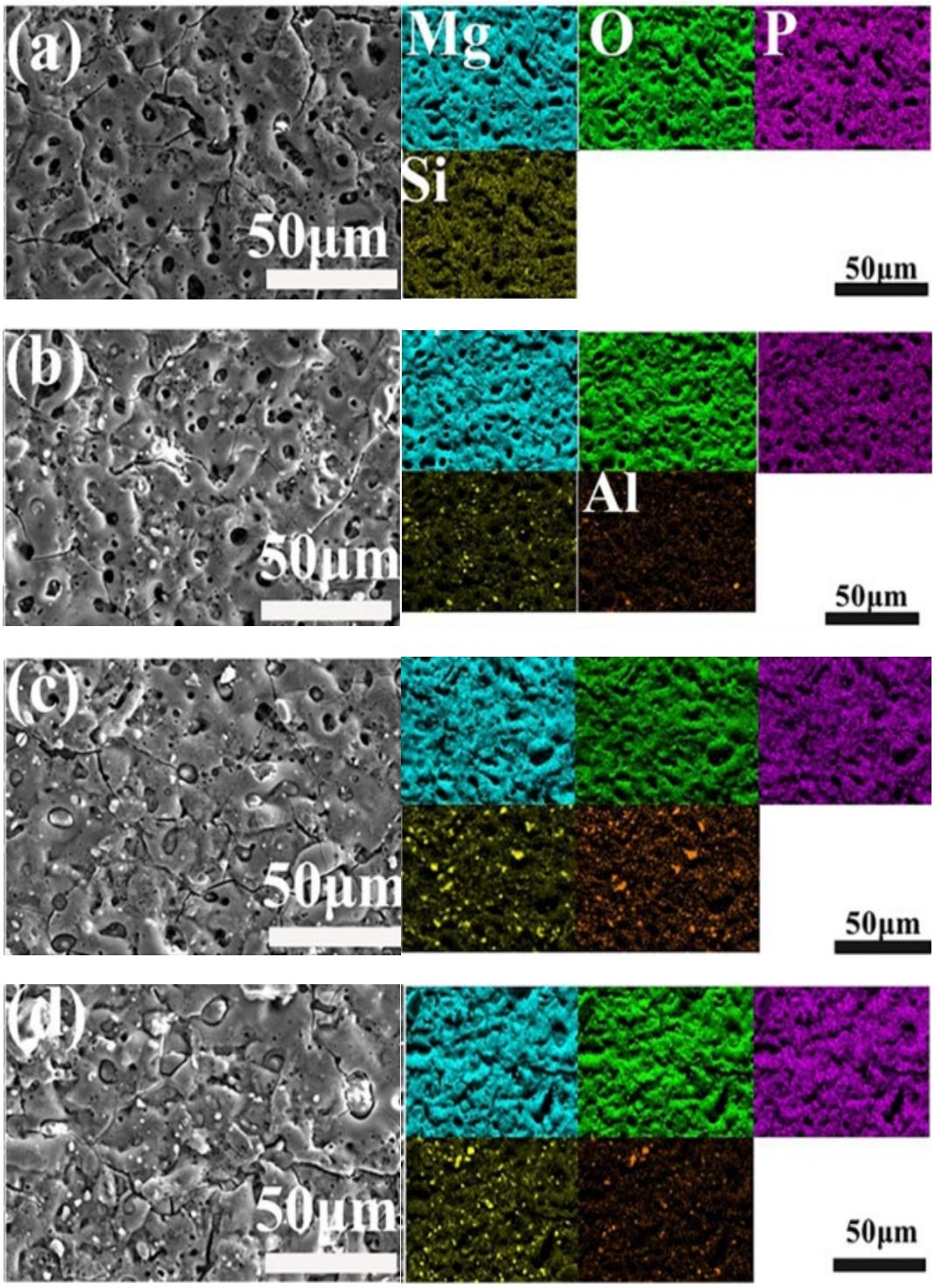

Fig. 4. SEM images and EDS analysis of different MAO samples.

Fig. 5 presents the SEM cross-sectional and EDS analysis of different coatings. As shown in Fig.5a, the cross-section of the NZP-0g coating contains numerous cavities, with some pores extending from the outer surface into the middle layer of the coating. The EDS analysis of NZP-0g reveals that the coating primarily consists of Mg, O, P, and Si. Fig.5-d demonstrate that with

increasing NZP content, the number of cavities and cracks extending from the outer layer inward decreases in the NZP-10g, NZP-15g, and NZP-20g coatings. Additionally, the location of the cavities shifts from the interior toward the outer region of the coating. A comparison of Fig.5d and 5a indicates that the NZP-20g coating exhibits significantly higher density than the NZP-0g coating.

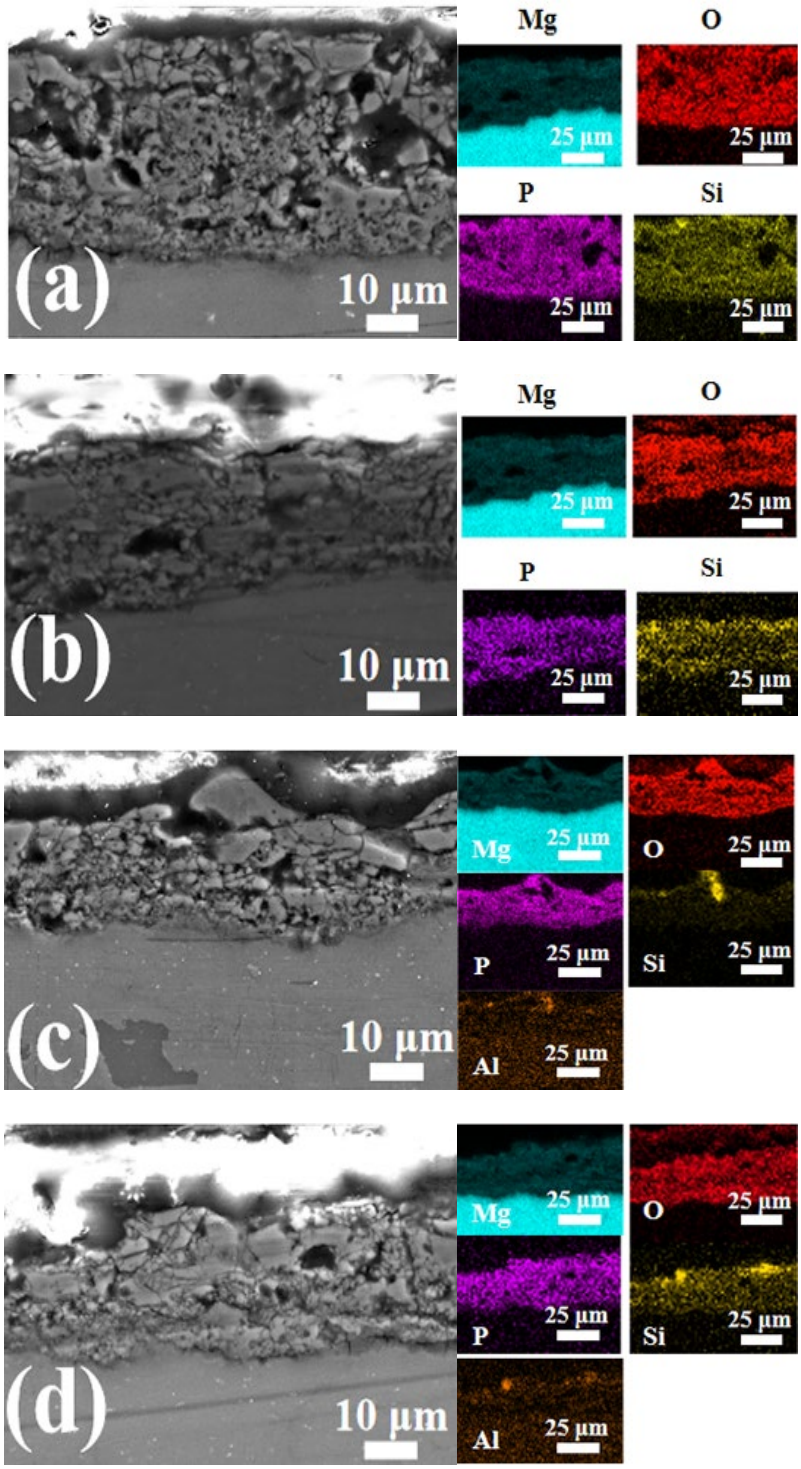

Fig. 5. SEM and EDS plots of different MAO sample cross sections.

The EDS analysis of the NZP-10g, NZP-15g, and NZP-20g cross-sections shows that the coatings are primarily composed of Mg, O, P, Si, and Al. Due to the low Ca content in NZP, it is not distinctly detected in the EDS results. With increasing NZP content, Al and Si elements become increasingly enriched at the cross-sectional surface and near the outer region of the coatings. It is indicated that NZP is both incorporated into the coating and adsorbed onto the surface. Based on these findings, the incorporation of NZP into the MAO layer occurs via two mechanisms: 1) NZP participates in the coating formation by embedding into the outer and inner surfaces of the coating. This mechanism helps seal larger pores and relieves residual stress in the coating, reducing the tendency for crack formation. 2) NZP does not directly contribute to coating formation but is adsorbed onto the outer surface during the solidification process. This mechanism primarily reduces small pores on the prepared surface.

Fig. 6 presents the polarization curves and electrochemical impedance spectroscopy (EIS) plots of different samples. From Fig.6a,we can see that the corrosion potentials of the samples from NZP-0g to NZP-20g are -1.51 V, -1.50 V, -1.42 V, and -1.50 V, respectively, indicating that the NZP content has a minimal impact on the corrosion potential and corrosion tendency. The calculated corrosion current density decreases from 7.32×10^{-6} A/cm² (NZP-0g) to 1.22×10^{-6} A/cm² (NZP-20g), representing an approximately sixfold reduction. A larger Nyquist arc radius corresponds to improved corrosion resistance[10].

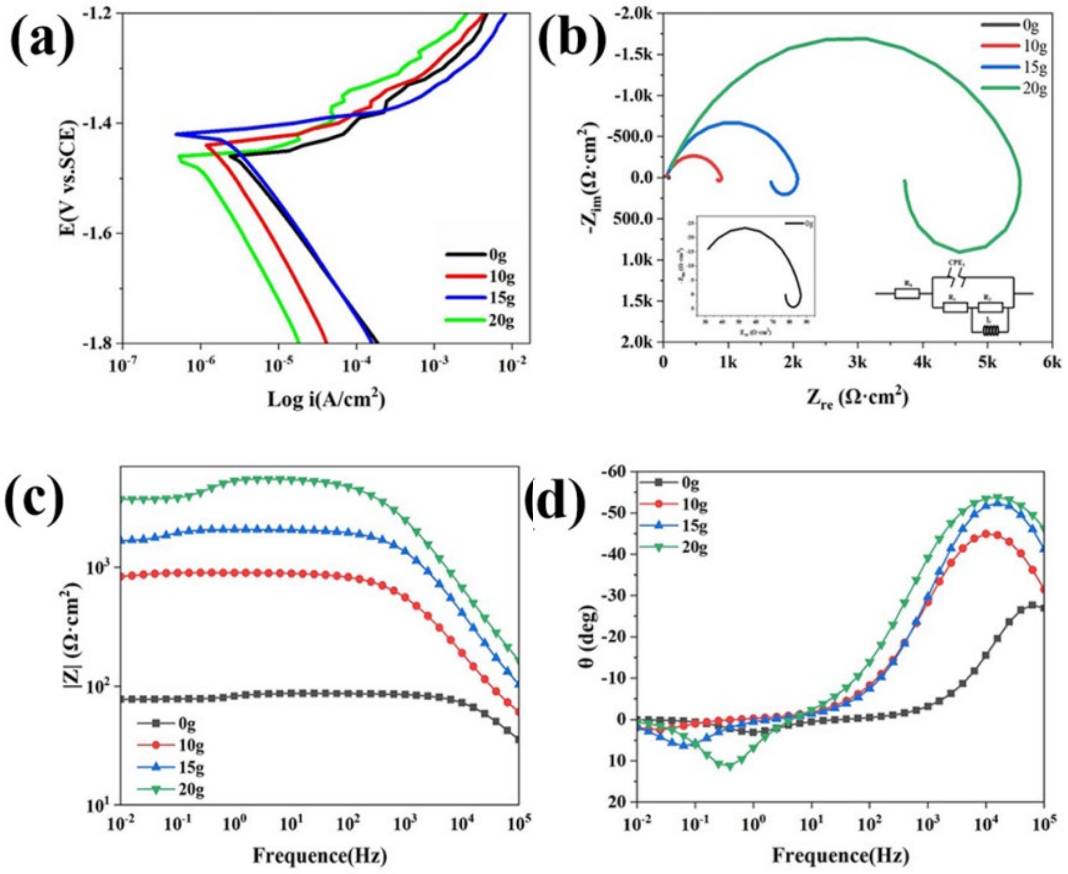

Fig. 6. Polarization curves and EIS results of different addition of NZP, a) Polarization curves. b)Nyquist plots. c) Bode-modulus diagrams. d) Bode-phase diagrams.

As evident in Fig.6b, the Nyquist arc radius of the coating increases progressively with the NZP content. The NZP-20g sample exhibits the largest capacitive reactance radius of 1.69×10^4 $\Omega\cdot cm^2$, which is approximately four orders of magnitude higher than that of NZP-0g (22 $\Omega\cdot cm^2$). In the Bode plots, there is a higher phase angle under high frequencies and greater impedance under mid-to-low frequencies indicate enhanced corrosion resistance[11]. As illustrated in Fig.6c and 6d, the increase in NZP content leads to an increase in high-frequency phase angle and mid-to-low-frequency impedance. At 10^5 Hz, the phase angle of NZP-20g reaches 46.2°, nearly twice that of NZP-0g (26.9°). At 10^{-2} Hz, the impedance $|Z|_{f=0.01}$ of NZP-20g increases by three orders of magnitude from 77.6 $\Omega\cdot cm^2$.

Fig. 7 presents the XRD patterns of different samples after immersion in 3.5 wt.% NaCl solution for 168 hours. As shown in the figure, the primary corrosion product formed after 168 hours is identified as $Mg(OH)_2$. With increasing NZP content, the peak intensities of the (011), (101), and (110) crystal planes of $Mg(OH)_2$ gradually decrease, indicating a reduction in the amount of $Mg(OH)_2$ formed due to corrosion. This result suggests that NZP contributes to enhancing the corrosion resistance of the MAO coating.

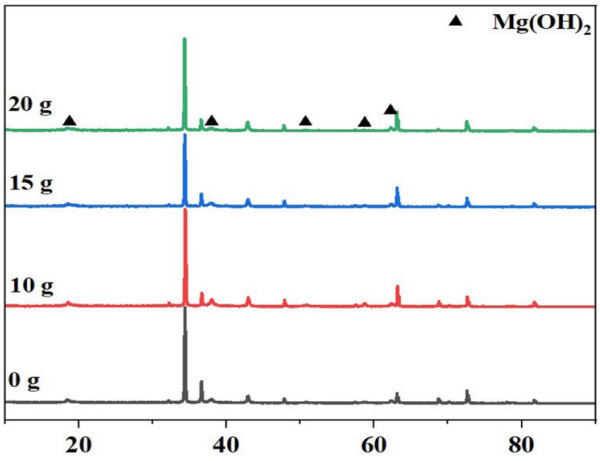

Fig. 7. XRD pattern after immersion in 3.5 wt.% NaCl solution for 168h.

Fig. 8 presents the SEM and EDS results of different specimen after immersion in 3.5 wt.% NaCl solution for 168 hours. As shown in Fig.8a we can see that there are pits and cracks, with visible of corrosion-induced spalling. However, as the NZP content increases, the surface pores of the coating become sealed, resulting in improved coating integrity. The SEM images at 1500× magnification reveal that during the corrosion process, NZP plays a crucial role in sealing pores, inhibiting crack propagation, and enhancing the cohesion of the protective coating. Typically, the degradation of the MAO coating is attributed to stress induced by volume changes caused by the precipitation of corrosion products from the coating. The corroded surface of the coating presents a network-like morphology with cracks and spalled fragments. However, with increasing NZP content, the stable integration of NZP within the MAO coating impedes the destructive effect of corrosion products. As shown in Fig.8c, in the NZP-15g coating, the embedded NZP inhibits crack formation even after the outer MAO layer has partially peeled off. Similarly, in Fig.8d, the NZP embedded in the MAO layer of the NZP-20g coating prevents coating detachment, confining corrosion to the

coating surface. This finding suggests that NZP mitigates stress cracking induced by the volumetric expansion of corrosion products. EDS analysis detected Cl, which may originate from magnesium chloride; however, its concentration is too low to be detected by XRD.

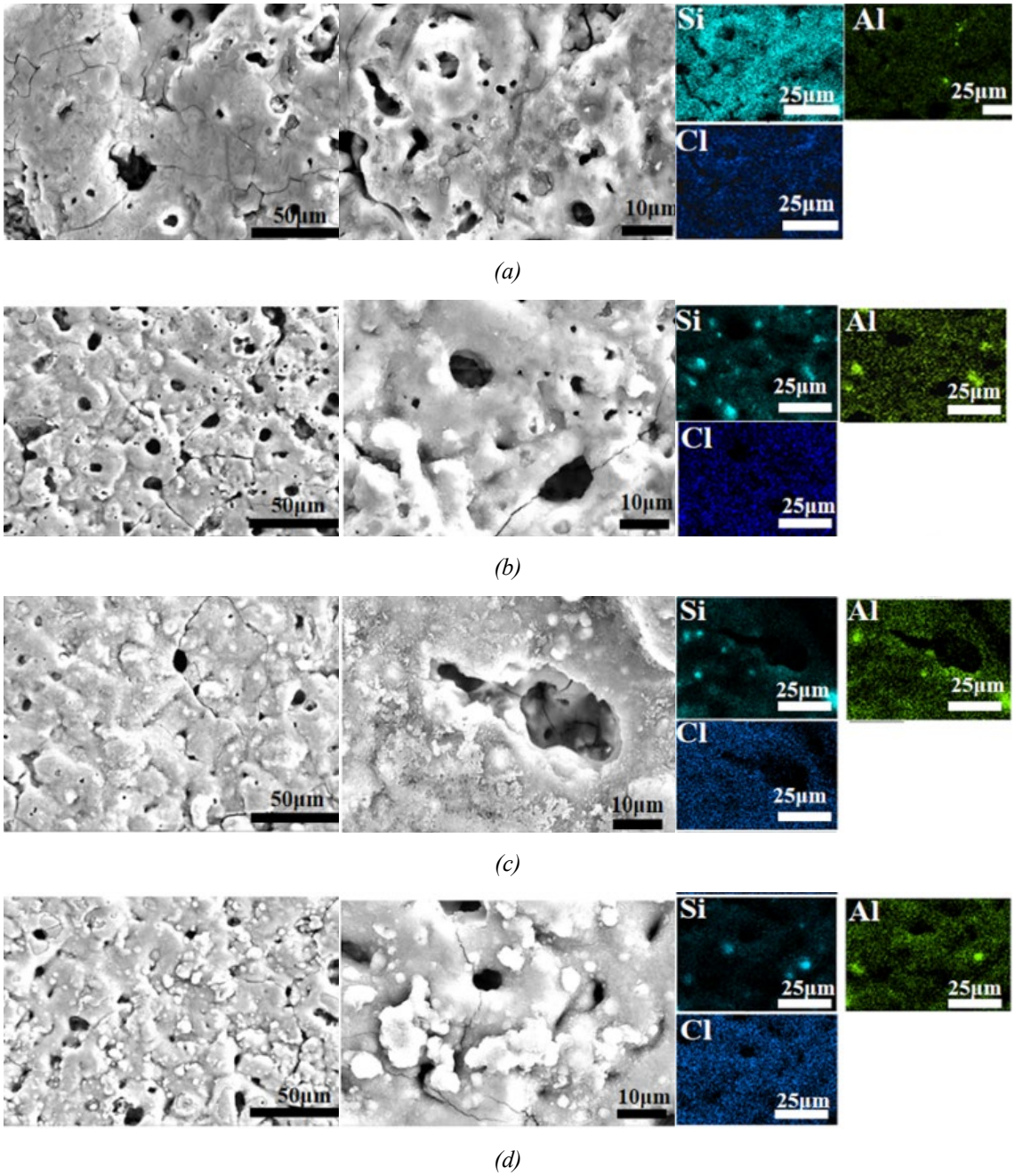

Fig. 8. SEM Morphology of corroded surface immersed in NaCl solution for 168h.

4. Conclusion

The addition of 20 g/L NZP into the electrolyte can make the MAO layer be enhanced pore-sealing properties. The reducing the porosity can be reduced from 15.78% to 7.4%. The self-corrosive current density is decreased from 7.32×10^{-6} A/cm² to 1.22×10^{-6} A/cm². Meanwhile, the

impedance is increased from 77.6 Ω·cm² to 3.72 × 10³ Ω·cm² with three orders of magnitude. The incorporation of NZP effectively can reduce the formation and accumulation of corrosive products when immersion on the surface. This approach, which utilizes untreated NZP, is both simple and cost-effective, contributing to resource efficiency and environmental sustainability.

Acknowledgments

The authors would like to acknowledge the financial support from the Science Program Project of Liaoning Provincial Department of Education JYTMS20230845.

References

[1] Dong HR, Li Q, Xie DB, Jiang WG, Ding HJ, Wang S, An LY (2023), Ceram. Int. 49(19): 32271-32281; https://doi.org/10.1016/j.ceramint.2023.07.202

[2] Askarnia R, Sobhani M, Zare M, Aghamohammadi H, Staji H (2023), J. Mech. Behav. Biomed. Mater. 141: 105784; https://doi.org/10.1016/j.jmbbm.2023.105784

[3] Wang J, Dou JH, Wang ZC, Hu C, Liu JR, Yu HJ, Chen CZ (2023), J. Alloys. Compd. 962:171172; https://doi.org/10.1016/j.jallcom.2023.171172

[4] Parichehr R, Dehghanian C, Nikbakht A (2021), J. Alloy. Compd. 876: 159995; https://doi.org/10.1016/j.jallcom.2021.159995

[5] Huang SY, Chu YR, Yang SH, Lee YL (2023), Surf. Coat. Tech, 475: 130164; https://doi.org/10.1016/j.surfcoat.2023.130164

[6] Jiang SQ, Zhang ZY, Wang D, Wen YQ, Peng N, Shang W (2023), J. Magnes. 11.4:1367-1380; https://doi.org/10.1016/j.jma.2021.07.027

[7] Chen YN, Wu L, Yao WH, Wu JH, Xie ZH, Yuan Y, Jiang B, Pan FS (2022), Surf. Coat. Technol. 451:129032; https://doi.org/10.1016/j.surfcoat.2022.129032

[8] Chen QQ, Lu XP, Serdechnova M, Wang C, Lamaka S, Blawert C, Zheludkevich ML, Wang FH (2022), Corros. Sci. 209: 110785; https://doi.org/10.1016/j.corsci.2022.110785

[9] Zhao C, Wang XW, Li CP, Liu Y, Sun S, Yang SS, Sun YC, Peng ZJ, Yu QL, Cai M, Yu, Zhou F, Liu WM (2024), Tribol. Int. 191(2024): 109126; https://doi.org/10.1016/j.triboint.2023.109126

[10] Liu DJ, Liu J, Liu GY, Xie YT, Duan ZF (2023), Coatings. 13.3: 643; https://doi.org/10.3390/coatings13030643

[11] Li CY, Guo L, Fan XL, Zeng RC, Chen DC, Zhi KQ (2020), Bioact. Mater. 5.2: 364-376; https://doi.org/10.1016/j.bioactmat.2020.02.008